ADVANCED ENERGY & SUSTAINABILITY RESEARCH
www.advenergysustres.com

Investigating the Existence of a Cathode Electrolyte Interphase on Graphite in Dual-Ion Batteries with $LiPF_6$-Based Aprotic Electrolytes and Unraveling the Origin of Capacity Fade

*Lukas Haneke, Felix Pfeiffer, Katharina Rudolf, Pranti Sutar, Masoud Baghernejad, Martin Winter, Tobias Placke, and Johannes Kasnatscheew**

This study elucidates the presence of a cathode electrolyte interphase (CEI) at graphite positive electrodes (PEs) and assesses its impact on the performance of dual-ion batteries, being promising candidates for cost-efficient and sustainable stationary energy storage. Indeed, electrolyte oxidation increases during charge (5 V vs $Li|Li^+$) for decreased C rates, that is longer duration at high state-of-charges (SOC) , but effective protection and evidence for CEI formation is missing as no increase in Coulombic efficiencies is observed, even with literature-known electrolyte additives like vinylene carbonate, fluoroethylene carbonate, or ethylene sulfite in a highly concentrated base electrolyte (4.0 M $LiPF_6$ in dimethyl carbonate) as reference. Via studying charged and pristine PEs by X-ray photoelectron spectroscopy, PF_6^--graphite intercalation compounds and cointercalated solvent molecules are identified, while indications for CEI are absent within 1000 charge/discharge cycles. Nevertheless, a high capacity retention of ≈94% (referring to 0.1C) is demonstrated. Affirmed by Raman spectroscopy and scanning electron microscopy, the active material remains structurally stable, suggesting capacity fading to be dominated by resistance rise at the PE, likely due to an electronic contact resistance from active material grain boundaries and/or from the interface between electrode particles and the current collector in course of high volume changes; as systematically derived by impedance spectroscopy.

1. Introduction

Dual-ion batteries (DIBs) with graphitic carbons as positive electrode (PE) are considered as alternative to state-of-the-art lithium-ion batteries (LIBs) for applications in stationary energy storage ("grid storage") as the PE active material is relatively cheap, nontoxic, and potentially sustainable.[1–4] In addition, aqueous electrode processing is an established electrode manufacturing process for graphite electrodes and can further increase sustainability by avoiding F-free binders and organic solvents. Although the gravimetric/volumetric energy content of graphite-based DIBs is not competitive to LIBs, DIBs can also operate highly reversibly with an extended cycle life.[1] A capacity retention close to 100% is shown over 500 cycles for graphite || lithium titanate and graphite || Li metal full cells with ionic liquid (IL)-based electrolytes;[5] achieving specific discharge capacities of the cathode of ≈50 mAh g^{-1} at a cutoff potential of 5.0 V versus $Li|Li^+$ (room temperature). Even higher discharge capacities of ≈90 mAh g^{-1} are achieved with highly concentrated electrolytes (HCEs), which in contrast to ILs are applicable with graphite negative electrodes (NEs).[6,7]

However, DIBs with graphite PEs demonstrate a Coulombic efficiency (C_{Eff}) ≤ 99%, apparently caused by continuous oxidative electrolyte decomposition/self-discharge particularly at low currents.[8–10] An electronically passivating and PF_6^--permeable cathode electrolyte interphase (CEI) at the graphite|electrolyte interface can be a promising approach to enhance C_{Eff} by suppressing electrolyte oxidation at the electrode surface and/or solvent cointercalation.

Nevertheless, the CEI existence is under debate and hardly investigated for graphite-based PEs. Contrary to lithium bis (trifluoromethanesulfonyl)imide (LiTFSI) and lithium bis (fluorosulfonyl)imide (LiFSI), large amounts of electrolyte decomposition products are observed via X-ray photoelectron spectroscopy (XPS) on the surface of graphite PEs for highly concentrated $LiPF_6$-based electrolytes in dimethyl carbonate (DMC)

L. Haneke, K. Rudolf, P. Sutar, M. Winter, T. Placke, J. Kasnatscheew
MEET Battery Research Center
Institute of Physical Chemistry
University of Münster
Corrensstraße 46, 48149 Münster, Germany
E-mail: johannes.kasnatscheew@uni-muenster.de

F. Pfeiffer, M. Baghernejad, M. Winter
Helmholtz Institute Münster
IEK-12
Forschungszentrum Jülich GmbH
Corrensstraße 46, 48149 Münster, Germany

The ORCID identification number(s) for the author(s) of this article can be found under https://doi.org/10.1002/aesr.202400330.

DOI: 10.1002/aesr.202400330

and ethylene carbonate (EC).[11] Performance improvements applying triallyl phosphate as electrolyte additives are ascribed to the formation of a CEI for a potassium-based graphite || MoS_2 cell setup.[12] Further studies report formation of a CEI in graphite||Li metal DIBs applying, for example, Al_2O_3 or LTO coatings or *via* $LiPF_6$-based HCEs.[13,14] In contrast, a recent transmission electron microscopy study points to the absence of an interphase on cycled graphite PEs with fluoroethylene carbonate (FEC) as cosolvent and low $LiPF_6$ concentrations of 1 mol L^{-1}.[15]

Brittle inorganic coatings most likely inhibit conduction of large anions as, for example, PF_6^- or $TFSI^-$, and are prone to cracking due to the volume expansion of up to 140% upon anion intercalation into graphite.[16] Elastic polymers as coating or electrolyte solvent are thus considered more suitable.[12] However, most solid-state polymer electrolytes suffer from low ionic conductivities and/or a limited oxidative stability not suitable for application up to 5 V versus $Li|Li^+$.[17–19] As consequence, suitable CEI-forming additives render a more promising approach to form a protective interphase.

This study investigates the electrode|electrolyte interface of a graphite PE in a hybrid capacitor graphite || activated carbon (AC) half-cell system. To exclude any reduction of electrolyte additives at the counter electrode (CE), the operating potential is set to 3.5–2.5 V versus $Li|Li^+$. Thus, the impact of electrolyte additives exclusively on the graphite working electrode (WE) is analyzed. Vinylene carbonate (VC), FEC, ethylene sulfite (ES), and the IL 1-Ethyl-3-vinylimidazolium bis(trifluoromethanesulfonyl)imide (VIm) are evaluated as potential CEI-forming additives for the graphite PE. FEC, ES, and VC are known to reductively decompose on LIB NEs, such as graphite or Si.[20–22] While a high oxidative stability is suggested for FEC,[23,24] VC oxidatively decomposes on graphite PEs at ≈4.7 V versus $Li|Li^+$.[25,26] FEC is used as cosolvent in carbonate-based electrolytes, whereas addition of ES effectively leads to enhanced discharge capacities in IL-based DIBs.[9,23,27] Nevertheless, their impact of CEI formation on graphite is not elucidated yet.

Here, surface layer formation is investigated via a systematic XPS study on charged and discharged graphite samples and supported by measurements of carbon and fluorophosphate reference compounds. Pure highly orientated pyrolytic graphite (HOPG) is investigated as a free-standing model electrode to exclude any influence of inactive materials (such as the binder) on the surface composition. The origin of long-term capacity fading at the PE is evaluated by galvanostatic charge/discharge cycling, electrochemical impedance spectroscopy (EIS), Raman spectroscopy, and XPS with the aim to unravel practical hurdles of graphite-based DIBs.

2. Results and Discussion

2.1. Analysis of Electrolyte Additives

The influence of the electrolyte additives FEC, ES, VC, and VIm on electrochemical performance is investigated via galvanostatic charge/discharge cycling. As the electrochemical performance sensitively depends on concentration changes of the electrolyte salt for HCEs, the molar concentrations of both, additives and Li salt, are kept constant. First-cycle C_{Eff} values of (81 ± 1)%, (80 ± 1)%, and (80 ± 2)% are observed for 4.0 M $LiPF_6$ in DMC (PF), PF + 0.1 M FEC, and PF + 0.1 M ES, respectively (**Figure 1**a). In addition, similar specific discharge capacities of ≈92 and ≈80–84 mAh g^{-1} in the 1st and 100th cycle do not suggest pronounced differences in the chemistry of electrolyte|cathode interface with FEC and ES as additive.

Successive decrease of the C_{Eff} with declining current between cycles 49 and 59 implies continuous oxidative side reactions at the graphite PE. This is affirmed by a considerable self-discharge over time (5% after 24 h, Figure S2, Supporting Information). Dissolution of the Al current collector or the stainless steel cell housing as a notable contribution to parasitic side reaction is excluded by inductively coupled plasma-optical emission spectroscopy (ICP-OES) measurements and calculation of accumulated irreversible capacities (Table S1, Supporting

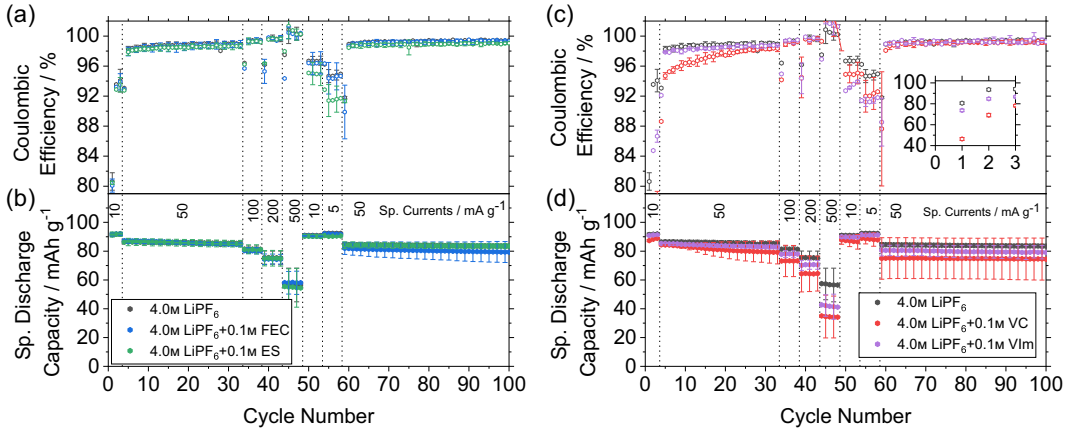

Figure 1. Galvanostatic cycling of KS6 graphite || AC half cells (5.0–3.4 V vs $Li|Li^+$, three-electrode Swagelok T-cells) with 4.0 M $LiPF_6$ in DMC (PF) and varied electrolyte additives. WE: KS6 graphite, CE: AC, and RE: Li metal. a,c) C_{Eff} and b,d) the specific discharge capacity versus cycle number. The applied specific currents are shown as inscriptions. The additive concentration of 0.1 mol L^{-1} corresponds to ≈0.5 wt% for VC, FEC, ES and to ≈2wt% for 1-Ethyl-3-vinylimidazolium bis(trifluorosulfonyl)imide (VIm).

Information). Therefore, these irreversible capacity losses are attributed to either internal oxidative decomposition of, for example, cointercalated solvent under reduction of the graphite intercalation compound (GIC) and continuous self-discharge or direct electrolyte oxidation at the graphite surface. Especially at low specific currents of 5 mA g^{-1} (≙0.05C) in cycles 54–58, a beneficial increase in C_{Eff} suggesting a better passivation is absent for PF + 0.1 M FEC ((94 ± 2)%) and PF + 0.1 M ES ((92 ± 1)%) compared to pure PF ((95 ± 1)%) and excludes any indications for an interphase. In contrast, lower first cycle C_{Eff} values compared to PF are achieved for PF + 0.1 M VC ((46 ± 1)%) and PF + 0.1 M VIm ((74 ± 1)%, Figure 1b), which likely originate from additional oxidative decomposition. Nevertheless, similar specific discharge capacities of ≈92 mAh g^{-1} and no improvement of the C_{Eff} at 5 mA g^{-1} are observed again. The high irreversible capacity for PF + 0.1 M VC reveals oxidation until VC is completely decomposed, which further hints on the absence of a protective interphase. In conclusion, no positive effects of the additives on the graphite|electrolyte interface and no indications for a protective layer are detected by galvanostatic experiments.

2.2. Surface Analysis of Cycled Graphite

Although no indications for an electrochemically effective CEI on the graphite PE were found in the previous section, an interphase not protecting in terms of parasitic redox processes may still be present. The general existence of an interphase is further studied via an XPS analysis of charged and discharged graphite. HOPG samples are charged to 5.0 V versus Li|Li^+ in HOPG || AC half cells containing pure PF. After rinsing the sample with pure DMC and direct transfer into the XPS chamber, it is measured after a waiting period of 2 h. The plateau in the potential profile at ≈4.8 V versus Li|Li^+ caused by the characteristic two-stage one transition (stage-wise occupation of graphite interlayer spaces during anion intercalation) and the reflecting blue color of the obtained GIC indicate the presence of a stage 1-GIC (Figure S3 and S4, Supporting Information).[28] Fast decrease in pressure to ≈10^{-8} mbar within 1 h indicates removal of residual solvent and a low initial content of volatile surface species. C 1*s*, F 1*s*, and P 2*p* spectra are depicted in **Figure 2**. To obtain additional information about the depth composition, Ar^+ sputtering is performed to successively remove the upper surface layer.

In the initial C 1*s* spectrum of the charged HOPG sample before Ar^+ sputtering (0 s, Figure 2a), a signal is observed at ≈283.1 eV with an asymmetric shoulder toward higher binding energy (BE). Fitting the spectrum with a peak model results in a prominent asymmetric peak at 283.1 eV which is assigned to a PF_6C_x GIC (for fitting parameters, see Table S2, Supporting Information). Upon sputter depth profiling (SDP) with Ar^+, this signal decreases and nearly vanishes for sputter times exceeding 360 s, while a peak at 284.3 eV gains intensity which is attributed to graphitic sp^2 carbon (*cf.* Table S5, Supporting Information). This is a strong evidence of sputter-induced degradation of the formed GIC. Decomposition of most organic and several inorganic compounds by Ar^+ sputtering and even low-energy sputtering methods using atom clusters has been shown in numerous reports.[29–32] A further peak close to the main signal is fit at 283.7–283.9 eV to achieve an accurate deconvolution of the C 1*s* spectrum. This peak is also attributed to a PF_6C_x phase. The signals with BE values lower than graphitic sp^2 carbon at 284.3 eV clearly indicate appearance of the PF_6C_x phases. The shift toward lower BE upon anion intercalation/oxidation is explained by removal of electrons from the graphite valence band and thereby a shift of the Fermi level to lower energy closer to the core electrons' states, that is, an increasing sample work function, which is also observed for intercalation of ClO_4^- into HOPG (**Figure 3**).[33] As the BE scale is referenced versus the energy of the Fermi level E_{Fermi}, the energy difference between

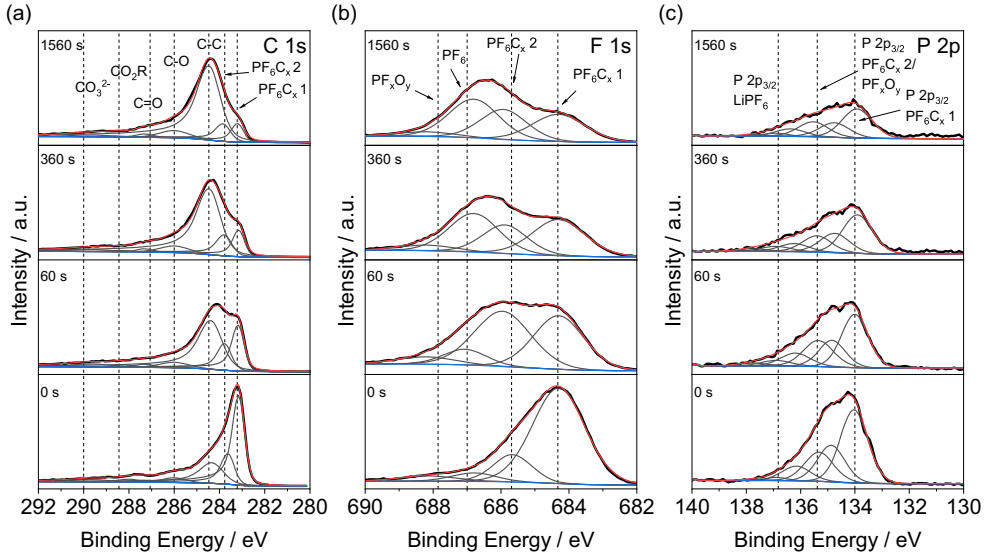

Figure 2. a) C 1s, b) F 1s, and c) P 2*p* XPS spectra of HOPG charged to 5.0 V versus Li|Li^+ at 2 mA g^{-1} (≙0.02C) in HOPG || AC cells (Swagelok three-electrode T-cells, half-cell setup). SDP is additionally performed at 0.5 kV with Ar^+ ions. Total sputter times are indicated as inscriptions in the stacked spectra. Measurements are performed without surface charge compensation. The highly conducting HOPG samples are directly clamped to a bare Cu sample holder to ensure good electronic contact.

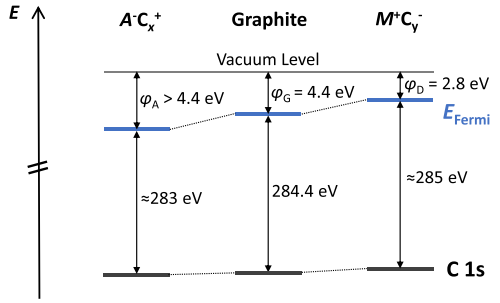

Figure 3. Schematic energy diagram for graphite, acceptor-type GICs ($A^-C_x^+$) and donor-type GICs ($M^+C_y^-$) modified from.[34] Anion intercalation/oxidation leads to removal of electrons from the valence band of graphite, while electrons are filled into the conduction band during cation intercalation/reduction, which leads to a shift of the Fermi level E_F toward lower/higher energy values, respectively. Consequently, the work function of the acceptor-type GIC (φ_A) is higher than that of graphite (φ_G), and the one for donor-type GICs (φ_D) is lower. Apart from the Fermi-level shift, the energy of the C 1*s* states is influenced by a chemical shift due to oxidation/reduction leading to an upshift/downshift.

the C 1*s* states (or other core orbitals of the analyzed phase) and E_{Fermi}, that is the measured BE of the transition, decreases. The opposite effect of an upshifting Fermi level/decreasing sample work function is described for pure LiC_6 and other alkali metal GICs.[34,35]

The C, P, and F elemental surface composition of the GIC sample (**Table 1**) reflects a stoichiometry of ≈PF_6C_{20} which is close to the expected one of PF_6C_{24} (for a deintercalation capacity of 93 mAh g^{-1}, see Figure 1) regarding that a minor amount of surface-adsorbed salt species as, for example, $LiPF_6$ of up to ≈1 at % may be present, as discussed in the following. No lithium signal can be detected at ≈56 eV, which in general partially overlaps with the loss structure of the F 2*s* transition (≥30 eV) complicating analysis for high F contents.[36] Therefore, minor Li impurities (up to ≈1 at%) may still be present that cannot be detected due to the error margin of the measurement. Still, the surface composition and the intensity of the PF_6C_x phases show that the amount of surface species present in the charged state is at the limit of detection.

According to the approximately reflected 'PF_6C_{24}' (stage 1) surface composition, the dominant peak 'PF_6C_x 1' at 283.1 eV is attributed to a stage 1 GIC. The 'PF_6C_x 2' phase at ≈283.7 eV has a smaller Fermi level shift compared to pristine HOPG and is therefore attributed to lower oxidation states, that is, higher GIC stages. It is noted that the fit 'PF_6C_x'peaks may contain multiple signals from C atoms located in different environments. Asymmetric peak broadening of the C 1*s* signal due to inequivalent carbon environments is for example reported for ultrahigh vacuum (UHV)-cleaved LiC_{18}.[37] The 'PF_6C_x 2' peaks may contain several GIC stages, which cannot be resolved here.

In the F 1*s* spectrum of the native GIC sample, a major peak assigned to intercalated PF_6^-, is observed at 684.3 eV (Figure 2b). While the LiF peak is expected at 685 eV,[38] the signal decrease upon Ar^+ sputtering, attributed to degradation of the GIC, and the negligible lithium content contradict the presence or formation of LiF, which is formed by $LiPF_6$ under UHV and by Ar^+ sputtering in particular.[39] Similar to the C 1*s* spectrum, a second intercalated PF_6^- component at ≈685.7 eV assigned to GICs with a higher stage is proposed. In the corresponding P 2*p* spectrum, P $2p_{3/2}$ peaks for stage 1 and higher staged PF_6C_x are detected at 134.0 and ≈135.3 eV, respectively (Figure 2c). For comparison, reference spectra of pristine $LiPF_6$ and $LiPO_2F_2$ are acquired (Figure S6, Supporting Information). Δ*BE* of the dominant P 2*p* and the F 1*s* signals for pristine $LiPF_6$ (Figure S6, Supporting Information) and intercalated PF_6C_x phases (Figure 2b,c) is approximately constant (**Table 2**), which hints on a similar chemical state of the anions.[40] Only the signals of the GICs are shifted toward lower BE compared to pristine HOPG and $LiPF_6$ due to the Fermi-level shift. This is in accordance to the results in previous studies showing that the chemical state of the anion is not notably changed upon intercalation.[10,41]

While the PF_6C_{24} stoichiometry is reflected by the elemental surface composition of P, C, and F, ≈10 at% of oxygen are observed in average which may originate from solvent decomposition products, adsorbed surface species, or cointercalated solvent molecules (Table 1). Cointercalation of ≈0.7 DMC molecules per GIC formula unit observed by dilatometry measurements for a $LiPF_6$-based electrolyte is reported in literature.[16] In the XPS O 1*s* spectra, the shoulder at 529.5 eV corresponding to 1 at% of oxygen cannot be correlated with the typical BE of organic oxygen species, but appears in the BE region related to metal oxides as, for example, Li_2O (Figure S7, Supporting Information).[29,42] However, notable amounts of salt species such as Li_2O (2 at% of Li for 1 at% of O) can be excluded due to the absence of a Li signal. Therefore, this shoulder is tentatively attributed to cointercalated DMC, as discussed in the following.

It is assumed that the signal shift to lower BEs observed for the F 1*s*, P 2*p*, and C 1*s* transitions of the 'PF_6C_x 1' phase compared to graphite and pristine $LiPF_6$ also applies to cointercalated DMC molecules. This shift equals ≈3 eV for the P 2*p* and F 1*s* signal of intercalated PF_6^- with respect to the signals for pristine $LiPF_6$.

Table 1. Elemental quantification of HOPG samples charged to 5.0 V versus Li|Li^+ in HOPG || AC half cells obtained from XPS spectra before Ar^+ sputtering.

Element	Rel. Surface Conc. [at%]	Ratio
F	19 ± 3	5.6
O	10 ± 2	2.9
C	67 ± 2	20
P	3.4 ± 0.3	1.0

Table 2. Peak positions of the main peaks in F 1*s* and P 2*p* XPS spectra and Δ*BE* values of the respective F 1*s* and P 2*p* peaks for the two observed main GICs, $LiPF_6$ and $LiPO_2F_2$.

Transition	PF_6C_x 1 [eV]	PF_6C_x 2 [eV]	$LiPF_6$ pristine [eV]	$LiPO_2F_2$ pristine [eV]
P $2p_{3/2}$	134.0	135.3	137.1	135.4
F 1*s*	684.3	685.7	687.2	687.9
Δ*BE*	550.3	550.4	550.1	552.5

Subtracting that shift from the BE of inorganic lithium carbonate's O 1*s* transition (≈532 eV) taken as approximation for the O1*s* signal of the volatile organic carbonate DMC, the result is close to the signal observed in O 1*s* spectrum of charged HOPG. The relative content of ≈1 at% would result in ≈0.3 cointercalated DMC molecules per unit PF_6C_{24}. However, it is possible that further signals from cointercalated DMC are convoluted within the main signal at 531–534 eV.

To investigate potential CEI formation on practical battery electrodes, XPS results of discharged KS6 graphite electrodes after three formation cycles at 10 mA g^{-1} (≙0.1C) are discussed. C 1*s*, F 1*s*, and P 2*p* spectra for a KS6 graphite electrode only immersed in PF and electrodes after formation using the PF electrolyte, PF + 0.1 M VC as oxidatively decomposing additive, and PF + 0.1 M ES are depicted in Figure S8, Supporting Information. ES chosen for XPS analysis as sulfur species can be directly correlated to additive decomposition products. However, no ES decomposition products indicating oxidative decomposition are found, which is in accordance to the electrochemical data. For all cycled samples, an intense graphitic C sp^2 peak at 284.3 eV and a small, convoluted shoulder at 283.8 eV, assigned to residual PF_6C_x according to the peak model established using HOPG, are observed in C 1*s* spectra. For the KS6 electrode only immersed in PF for 5 min and washed with DMC, signals in the F 1*s* spectrum at ≈686.5 eV and in the P 2*p* spectrum at ≈136.6 eV with a BE difference similar to that of $LiPF_6$ are observed (550.1 eV, *cf.* Table 2 and Figure S8, Supporting Information). Thus, the signal is tentatively attributed to surface-adsorbed PF_6^-. The F 1*s* and P 2*p* spectra of all cycled samples exhibit a maximum at ≈686 and ≈136 eV, respectively (Figure S8, Supporting Information). According to the peak model, these signals mainly consist of the 'PF_6C_x 2' phases with peak fit functions at ≈685.7 and ≈135.6 eV. A shoulder in the F 1*s* spectra at ≈688 eV present for all samples is assigned to fluorophosphates PF_xO_y according to the measurement of reference compounds (see Figure S6, Supporting Information). Apart from the small shoulder of fluorophosphates, additional decomposition products were neither detected for samples obtained using PF or PF + 0.1 M ES nor for the ones applying decomposing additives as VC. Analysis of oxidative VC decomposition via online electrochemical mass spectrometry on ^{13}C-labeled carbon electrodes reported in literature revealed extensive generation of CO_2 generation for ≥4.5 V versus Li|Li^+, and formation of poly(VC) was proposed.[43] The XPS results presented here, however, negate the appearance of insoluble polymers generated at the graphite surface for the used HCEs. This may be either explained by generation of smaller, soluble VC oligomers, which are removed during pretreatment before XPS analysis or by different decomposition products than proposed for $LiNi_xCo_yMnzO_2$ (NCM) PEs.

It becomes obvious from the small changes in surface composition upon cycling (**Figure 4**a) and from the intense, narrow graphitic C sp^2 signals comparable to that of the pure reference graphite samples (see Figure S5, Supporting Information) that the surface coverage after three formation cycles is very small for all of the electrolytes. In comparison to the pristine and the soaked electrodes, relative C concentrations decrease from ≈83 to ≈77 at% and F concentrations increase from ≈2 to ≥5 at% (Figure 4a). Compound quantification by peak fitting of F 1*s* spectra reveals that the main difference between the soaked and the cycled electrodes is the residual amount of intercalated PF_6^- as well as an increase of fluorophosphates, that is, actual decomposition/hydrolysis products for the cycled electrodes (Figure 4b). For the soaked electrodes, the relative fractions of PF_xO_y and PF_6C_x are negligible (≤0.5 at%). The low fraction of PF_6C_x accords with the fact that anion intercalation does not occur by simple immersion into the electrolyte.

For HOPG samples, the XPS spectra are acquired on the basal planes; thus, different compositions may principally be observed for the prismatic edge planes as reported for Li^+ intercalation into graphite.[44] In contrast, prismatic edges are considered to be more exposed to the X-ray beam for KS6 graphite electrodes due to different particle orientations and a high percentage of the nonbasal surface area,[45] although the flake-like particle shape may introduce a preferred orientation of basal planes parallel to the current collector.

As the overall amount of decomposition products is very low, strong coverage of only the prismatic edges is unlikely.

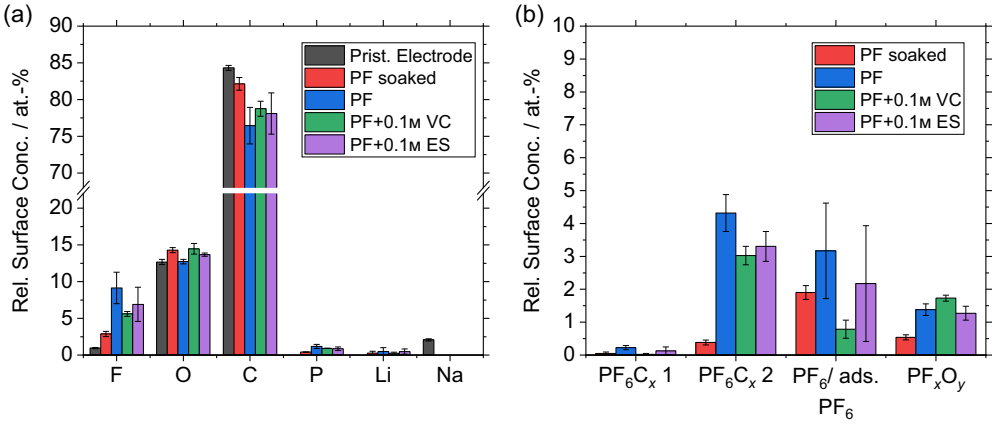

Figure 4. a) Elemental surface compositions of a pristine (Prist.) KS6 graphite electrode, a graphite electrode, that was immersed in PF (PF soaked) for 5 min and electrodes from cycled graphite || AC half cells after formation at 10 mA g^{-1} (≙0.1C, 5.0–3.4 V vs Li|Li^+). b) Compound quantification based on F 1*s* peak fitting for the respective electrolytes. For fitting parameters, see Table S2, Supporting Information.

Assuming a homogeneous surface coverage with $LiPF_6$ and fluorophosphate decomposition products, an apparent surface layer thickness d is calculated as a rough estimation according to the literature for the soaked and the cycled electrode using the PF electrolyte.[31] For this, the ratio of the relative carbon surface concentration of the respective sample (I) to that of the pristine electrode (I_0) was used.

$$d = \ln\frac{I_0}{I}\lambda_e t_f \cos_e\theta \quad (1)$$

The factor $t_f = 0.67$ accounts for the spherical particle shape, while the angle of emission for photoelectrons θ was 0°.[31] An average inelastic mean free path λ_e was calculated for a surface layer consisting of $LiPF_6$ ($\lambda_e = 3.59$ nm) and $LiPO_2F_2$ ($\lambda_e = 3.44$ nm) in the observed ratios from Figure 4b using the so-called TPP-2M method[46] and the United States National Institute of Standards and Technology (NIST) database calculation tool.[47] Calculation results in an apparent layer thickness of 0.6 ± 0.3 Å for the soaked sample and 2 ± 1 Å for the electrode cycled in PF. These values, obtained as an average defined by the general XPS measurement area of ≈700 µm × 300 µm, are lower than a single-atom layer of PF_6^- (effective ionic radius of ≈2.5 Å)[48] for the immersed sample. For the cycled sample obtained using PF, the values are in the range of a single-atom layer. In conclusion, only a minor amount of insoluble surface species, too low in amount for formation of a homogeneous surface layer, can be observed on the graphite surface via XPS in the charged and discharged state. The surface species most likely arise from $LiPF_6$ and its hydrolysis products.

2.3. Long-Term Galvanostatic Cycling and Impedance Analysis

To investigate potential formation of an interphase at the graphite|electrolyte interface during continuous cycling, galvanostatic long-term experiments (1000 cycles) at 100 mA g^{-1} (≙1C) with EIS measurements after formation and after a characterization cycle at 0.1C each 100th cycle are conducted in graphite || AC half cells. The specific discharge capacity and the C_{Eff} is plotted in **Figure 5** as a function of cycle number.

The long-term cycling experiment reveals a high reversibility with an average C_{Eff} of (99.74 ± 0.02)% from the 100th to the 1002nd cycle at 1C excluding all characterization cycles at 0.1C and their respective subsequent cycle (Figure 5a). In the third cycle at 0.1C, a specific discharge capacity of (96 ± 1) mAh g^{-1} is observed, while (89 ± 1) mAh g^{-1} is displayed in the fifth cycle at 1C (Figure 5b). A capacity retention of (94 ± 1)% is observed at 0.1C in the 903rd cycle with respect to the third cycle. At 1C in the 905th cycle, a capacity retention of (85 ± 3)% is found with respect to the fifth cycle (1C), which is substantially lower compared to the capacity retention at 0.1C. Therefore, it is concluded that the capacity fading is mainly driven by kinetic hindrance caused by, for example, passivation of interfaces at the WE as discussed in the following. This is affirmed by the evolution of overpotentials, being after ≈900 cycles more pronounced for cycling at 1C compared to cycling at 0.1C as observed in the corresponding potential profiles (Figure S9, Supporting Information).

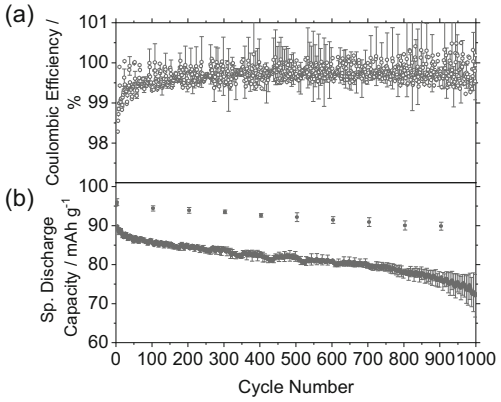

Figure 5. Galvanostatic cycling of graphite || AC half cells (5.0–3.4 V vs Li|Li^+, three-electrode PAT cell format) using 4.0 M $LiPF_6$ in DMC. WE: graphite, CE: AC, and RE: Li metal. a,b) The C_{Eff} and the specific discharge capacity versus cycle number, respectively. Three formation cycles were performed at 10 mA g^{-1} (≙0.1C). Long-term cycling was performed at 1C. Every 99 cycles, a characterization cycle was performed at 10 mA g^{-1} with a subsequent EIS measurement after charging to 4.6 V versus Li|Li^+ at 10 mA g^{-1}. Small capacity and C_{eff} fluctuations are caused by minor temperature deviations ((22 ± 1) °C).

For further insights, impedance spectra are analyzed (**Figure 6**). The spectra are recorded in the anion intercalation potential region at 4.6 V versus Li|Li^+ to ensure nonblocking conditions, that is, to include the impedance response of the charge transfer reaction.[49]

In cycle 4, the impedance plot exhibits a small tail at high frequency from ≈10 kHz to 1 kHz (see Figure 6b, 22 Ω ≤ Re(Z) ≤ 23 Ω), a straight region at a ≈45° angle in the midfrequency region (≈1 kHz–10 Hz) and a steep increase of the imaginary part below 10 Hz (Figure 6a,b). With continuous cycling, the small feature at ≈10–1 kHz evolves into a depressed semicircle with growing radius. Impedance spectra of pristine graphite electrodes show an impedance response typical for porous electrodes under blocking conditions (at open-circuit potential), which can be approximated with a so-called reflecting transmission line model (TLMR).[49–51] A detailed derivation of observed impedance features and validation of the half-cell measurement setup using pristine and charged graphite electrodes at different SOCs is described in the SI.

It is found that the depressed high-frequency semicircle is not related to the charge transfer process during anion intercalation, but is also present in the discharge state (Figure S10, Supporting Information). The absence of visible charge transfer features as a separate semicircle may be related to a more complex impedance composition that cannot be approximated with simple passive circuit elements or a very small charge transfer resistance as shown for anion intercalation for aqueous electrolytes.[52] In consequence, the evolving high-frequency arc (Figure 6) is related to a growing layer of unknown morphology that introduces an additional contact resistance R_{cont} and a double-layer capacitance. As schematically depicted in **Figure 7**, this layer may be present on 1) the electrochemically active surface of the graphite PE, similar to the SEI for NEs, at 2) the interfaces between active material particles, 3) the current collector|electrode coating interface,[53]

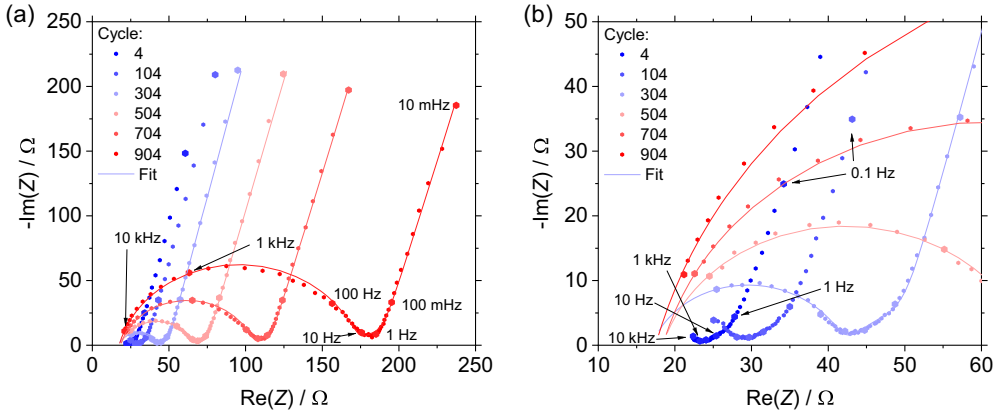

Figure 6. a) Impedance spectra (10 kHz $\geq f \geq$ 10 mHz, 10 mV amplitude) obtained in the nonblocking state after formation and every 100 cycles during long-term galvanostatic cycling experiment of graphite || AC cells at 100 mA g^{-1} (5.0–3.4 V vs Li|Li^+, PAT three-electrode cell, half-cell setup) using PF. b) Magnification of the high-frequency region of spectra depicted in (a). To achieve nonblocking conditions, the WE is charged to 4.6 V versus Li|Li^+ with a following rest step of 2 h before the impedance measurements. Spectra are fit with a transmission line model depicted in Figure 8 starting from the 300th cycle due to the ambiguity of the fit in the high-frequency region at lower cycle numbers.

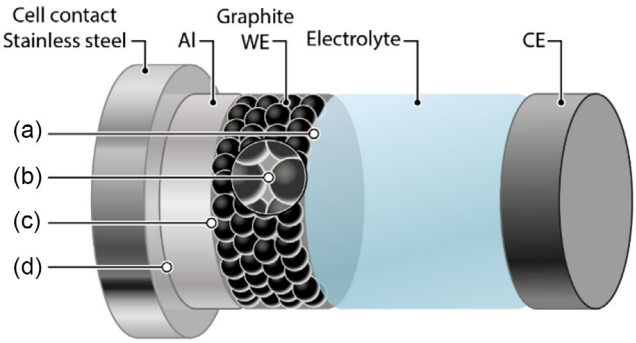

Figure 7. Schematic illustration of interfaces at the PE: a) the graphite|electrolyte interface, b) the grain boundary interface, c) current collector|electrode coating interface, and d) the interface between current collector and the stainless steel cell housing.

or 4) the interface between the backside of the Al current collector and the cell's stainless steel contact by, for example, creeping electrolyte. It is supposed that in case (a), R_{cont} is an ionic resistance, as anions have to penetrate through such an interphase for charge transfer. In the cases (b)–(d), the electronic transport is affected, which would result in an electronic R_{cont}.

To investigate the origin of this arc evolving with continuous cycling, the impedance spectra are fit with an equivalent circuit model. The high-frequency semicircle is fit with a parallel combination of a contact resistance R_{cont} and a constant phase element (CPE) termed CPE_{cont} with the CPE value Q_{cont} and the CPE exponent α to account for the additional double-layer capacitance. The impedance of the CPE $Z_{CPE,cont}(\omega)$ at an angular frequency ω (with imaginary unit i) is given by

$$Z_{CPE,cont}(\omega) = \frac{1}{Q_{cont}(i\omega)^{\alpha}} \quad (2)$$

The mid- to low-frequency region presumably determined by restricted diffusion of anions within the graphite particles[54] (see Supporting Information) is fitted with a TLMR.[55,56] Quantification results obtained from impedance fits are presented in **Figure 8**.

While R_{el} is nearly constant as expected (Figure 8a), R_{cont} increases substantially from (26 ± 2) to $(221 \pm 70)\,\Omega$ and is the greatest contribution to the real part of the impedance (Figure 8b). R_{TLMR} increases from $(23 \pm 1)\,\Omega$ in the 304th cycle to $(69 \pm 24)\,\Omega$ in the 904th cycle (Figure 8d). Its physical origin, here assigned to the finite anion diffusion process within graphite, cannot be explained without ambiguity, though, as it may be possible that mass transport processes in the electrolyte also contribute to the low-frequency impedance.[49]

To obtain further information about the additional layer introducing R_{cont}, the effective capacitance $C_{cont,\,eff}$ is calculated from the CPE value Q_{cont} by the Brug equation (Equation (3)).[57,58] This is performed because a CPE (see Equation (2)), used to describe the impedance of non-ideal electrochemical double layers, is a mathematical construct whose parameter Q_{cont} does not have a direct physical meaning for $\alpha < 1$ (ideal capacitor: $\alpha = 1$).[57] In the physically motivated model by Brug et al. the impedance of, for example, a film at an electrode|electrolyte interface is described as parallel network of r_{el}–$r_f||c$ branches (r_{el}: electrolyte resistance element, r_f: film resistance element, c: capacitance element) to account for a distribution of local capacitance elements over the surface.[57,58]

$$C_{cont,\,eff.} = \left(\frac{R_{el}R_{cont}}{R_{el}+R_{cont}}\right)^{\frac{1-\alpha}{\alpha}} Q_{cont}^{\frac{1}{\alpha}} \quad (3)$$

$C_{cont,\,eff}$ slightly rises from $(1.0 \pm 0.2)\,\mu F$ (cycle 304) to $(1.5 \pm 0.1)\,\mu F$ (cycle 904, Figure 8d), which equals $\approx 0.4 - \approx 0.6\,\mu F\,cm^{-2}$ relative to the geometric electrode area (2.56 cm^2).

For a layer of thickness d that homogeneously coats the active material particles (i.e., covers a constant area A), the capacitance C of the layer is expected to decline with growing layer resistance by thickness increase due to $C \approx A/d$ for an ideal plate capacitor.

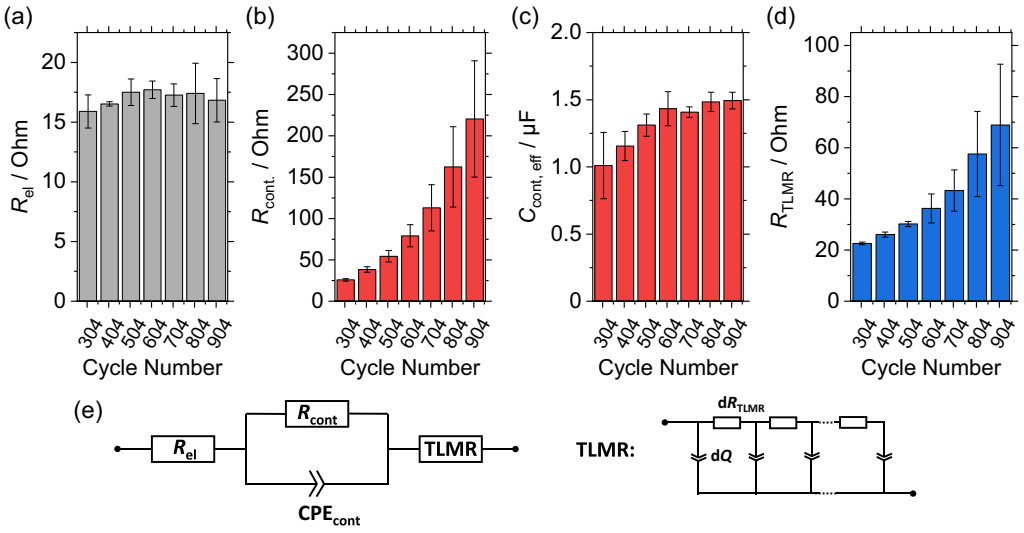

Figure 8. Quantification results of a) the Ohmic resistance contributions by the electrolyte and electronic contacts R_{el}, b) the contact resistance R_{cont} related to the evolving high-frequency arc, c) the corresponding effective capacitance $C_{cont, eff}$ (calculated from Q_{cont} of CPE_{cont} as described below), and d) the total resistance R_{TLMR} of the TLMR. An illustration of the equivalent circuit model is depicted in e).

The increasing $C_{cont, eff}$ is interpreted as increasing interfacial area at the location of the contact resistance. Therefore, a homogeneous coating of the electrochemically active surface area of graphite is unlikely.

Furthermore, impedance spectra are recorded at varying temperatures (Figure S13, Supporting Information). By comparing the temperature dependency of the obtained resistance via the Arrhenius equation, ionic and electronic resistances can be distinguished.[53,59] Electronic resistances increase minimally with temperature and exhibit a low activation energy <1 kJ mol^{-1} whereas the activation energy for ionic and mass transport-related resistances is an order of magnitude higher ($\approx$15 kJ mol^{-1}), and their resistances notably decrease with rising temperature.[53,59] As shown in Figure S13, Supporting Information, R_{el} and the low-frequency TLMR impedance are substantially reduced upon temperature increase from 10 to 40 °C, while the radius of the high-frequency arc corresponding to R_{cont} is nearly constant. This shows that R_{cont} is an electronic resistance and is not related to the electrode|electrolyte interface.

In summary, no evidence for formation of a protective CEI-like interphase at the graphite PE|electrolyte interface can be found, which is in accordance to the XPS results. Even after 1000 cycles, hardly any electrolyte decomposition products can be identified on the surface of graphite electrode via XPS (Figure S14 and S15, Supporting Information).

As mentioned, a further origin of the evolving contact resistance may be the passivation of the interface between the cell housing's stainless steel contact and the Al current collector by, for example, creeping electrolyte. Crystallization of $LiPF_6$ can be related to the high salt concentration in the HCE, which may increase with solvent decomposition or minor solvent loss through the fittings of the cell housing during long-term experiments. To analyze whether R_{cont} is caused by crystallization of electrolyte salt at the current collector back side, a discharged graphite electrode was extracted from a cell cycled for 1000 times and was thoroughly rinsed with DMC from both sides in a glovebox. The rinsed electrode was then assembled into a new cell with a fresh separator, CE, and electrolyte for an impedance measurement (Figure S16, Supporting Information). As the radius of the depressed semicircle located at $10\,\Omega \leq \mathrm{Re}(Z) \leq 1000\,\Omega$ after formation and after 1000 cycles is comparable, it is concluded that R_{cont} was not notably affected by the washing procedure. Hence, salt crystallization can be disregarded as the origin for R_{cont}. Furthermore, no evidence for growth of the electronic passivation layer on the Al-current collector backside was observed by XPS during galvanostatic long-term cycling Figure S17, Supporting Information.

In conclusion, R_{cont} can be attributed to the grain boundaries within the electrode coating or to the current collector|electrode coating interface. The reason may be, for example,, successive loss of direct contact between particles or particles and the current collector caused by the repeated large volume changes of $\approx$140% upon de–/intercalation.[16,60]

2.4. Structural Investigation of Cycled Graphite

To investigate whether the graphite active material or the electrode morphology structurally degrade after extended cycling, KS6 graphite electrodes are analyzed by scanning electron microscopy (SEM) (**Figure 9**).

While the flake-like graphite particles are loosely packed in the pristine state (Figure 9a), less voids between the particles are observed for electrodes after formation (Figure 9b,c) and after 1000 cycles (Figure 9d,e). This is attributed to a slight compaction of the uncalendered graphite electrodes in the initial cycles related to the pressure on the cell stack and graphite volume changes during anion de-/intercalation. Apart from that, neither the overall electrode morphology nor the particle morphology changes notably after extended cycling. No surface coverage

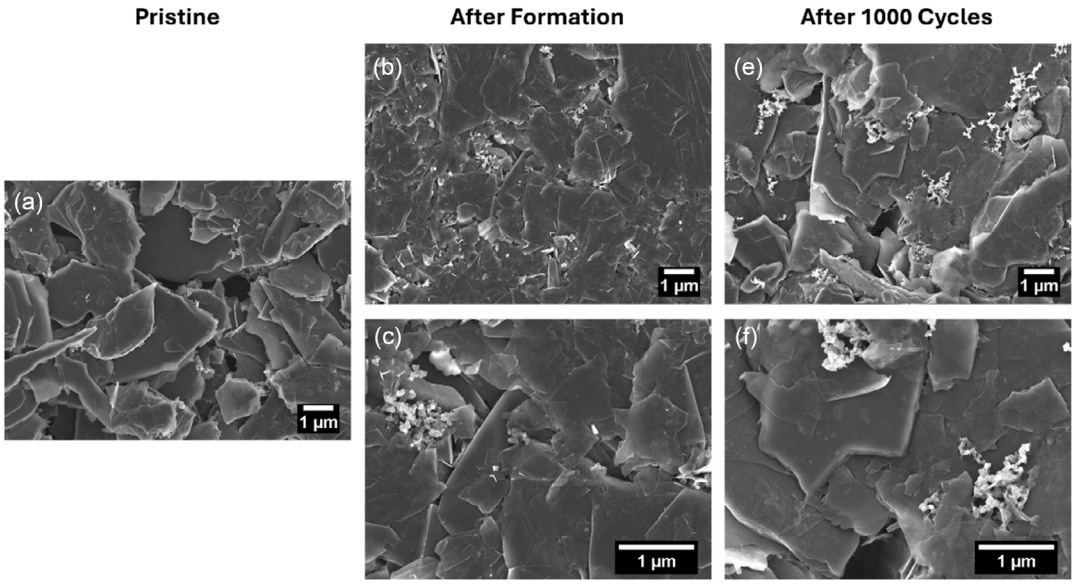

Figure 9. SEM micrographs of a KS6 graphite electrode a) in the pristine state, b,c) after three formation cycles at 10 mA g^{-1} (0.1C), and d,e) after 1000 cycles at 100 mA g^{-1} in graphite || AC half cells (5.0–3.4 V vs Li|Li^+).

by, for example, electrolyte decomposition products is observed in accordance to the previous results.

To further examine structural active material degradation, Raman spectra are acquired of pristine and cycled graphite electrodes (**Figure 10**a).

For all samples, a small peak ascribed to the graphite *D*-band at ≈1352 cm^{-1} and an intense graphitic *G*-band signal at ≈1583 cm^{-1} is observed. The *G*-band originates from bond stretching of sp^2 carbons (E_{2g} mode), while the *D*-band is attributed to a breathing mode of the C—C sp^2 rings, that is only present in the vicinity of crystal defects.[61,62] The small shoulder at ≈1620 cm^{-1} observed for all samples is attributed to the *D'*-band, which shows that the pristine graphite electrode also exhibits crystal defects.[61] Whereas the intercalation of anions has no influence on the *D*-band, the *G*-band is split and exhibits a shift to higher wavenumbers upon intercalation. The band at ≈1583 cm^{-1} is assigned to the mode of the inner graphene layers of higher-stage GICs, $E_{2g}(i)$, and the peak at ≈1606 cm^{-1} to that of the outer graphene layers adjacent to intercalate layers $E_{2g}(o)$.[63,64] In accordance with the XPS results, both the electrode after formation and the one after 1000 cycles still contain residual intercalated anions (Figure 10a). The slightly higher amount of anions for the sample after long-term cycling may be related to the kinetic hindrance evolving as discussed.

Several stages have been proposed in literature for the introduction of disorder into graphitic carbons: 1) particle size

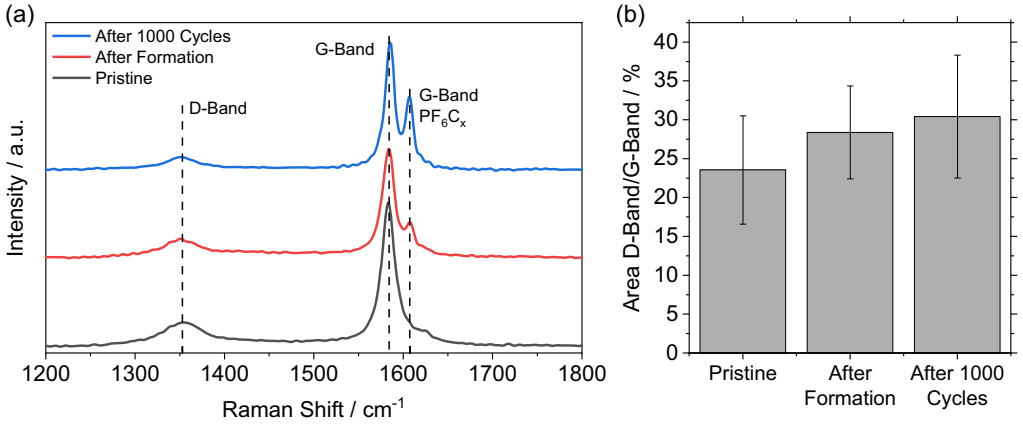

Figure 10. a) Raman spectra of KS6 graphite electrodes in the pristine state, after formation and after 1000 cycles in the discharged state extracted from graphite || AC half cells (5.0–3.4 V vs Li|Li^+). b) Comparison of relative peak areas of *D*-band to *G*-band. For formation, three cycles were conducted at 10 mA g^{-1} (0.1C). Two samples aged for 1000 cycles were obtained from long-term experiments at 100 mA g^{-1} with a characterization cycle and EIS measurement every 100 cycles.

reduction, that is, formation of nanocrystalline graphite and 2) transition of sp^2 carbon to amorphous sp^3 carbon. While the peak area ratio of *D*-band to *G*-band (*D*/*G*) increases at stage (1), it decreases with a greater degree of disorder for a high defect concentration and crystallites smaller than 3 nm (2).[62] However, the *G*-band's full width at half maximum (FWHM) generally rises with evolving disorder for both stages, which allows differentiation of the two steps.[65]

Here, the *D*/*G* ratio does not notably change within the measurement error margin after formation and after 1000 cycles compared to the value for pristine samples (Figure 9b). In addition to that, neither a distinct broadening of the *G*-band for the inner, nonintercalated graphene layers (Figure 10a), nor a significant FWHM increase of the C sp^2 peak in XPS C 1*s* spectra after 1000 cycles (≈0.6 eV for samples after formation and samples extracted from cells after 1000 cycles, see Figure S10 and S16, Supporting Information) is detected. Together with the absence of notable adventitious sp^3 carbon signals in the XPS C 1*s* spectra, it is concluded that no hints on structural degradation of graphite are present even after extensive cycling in a half-cell setup using PF. The observed capacity fading is therefore mainly attributed to kinetic hindrance by formation of an electronic contact resistance.

3. Conclusion

The electrode|electrolyte interface of graphite PEs in DIBs is systematically investigated via electrochemical techniques and XPS. The additive impact of fluoroethylene carbonate (FEC), ethylene sulfite (ES), vinylene carbonate (VC), and 1-ethyl-3-vinylimidazolium bis(trifluorosulfonyl)imide (VIm) in 4.0 M $LiPF_6$ in DMC (PF) on CEI formation is analyzed. While vinylene carbonate VC and VIm oxidatively decompose during cycling, no indications of oxidation are found for FEC and ES. Nevertheless, independent of oxidation reactions and additives, an improvement in Coulombic efficiency (C_{Eff}) and passivation indications are not observed, as schematically shown in **Figure 11**. Investigation of the chemical composition at the graphite|electrolyte interface is performed via XPS. Using charged HOPG as well as carbon and fluorophosphate reference compounds, the XPS peak positions of a stage 1 phase, most likely originating from PF_6C_{24}, and higher GIC stages are identified in C 1*s*, F 1*s*, and P 2*p* spectra. In accordance with literature, GIC signals are shifted up to 3 eV toward lower values compared to the pristine components caused by a shift of the Fermi level. Strong hints on cointercalation of solvent molecules are found due to a shifted oxygen peak observed in O 1*s* spectra. Hardly any

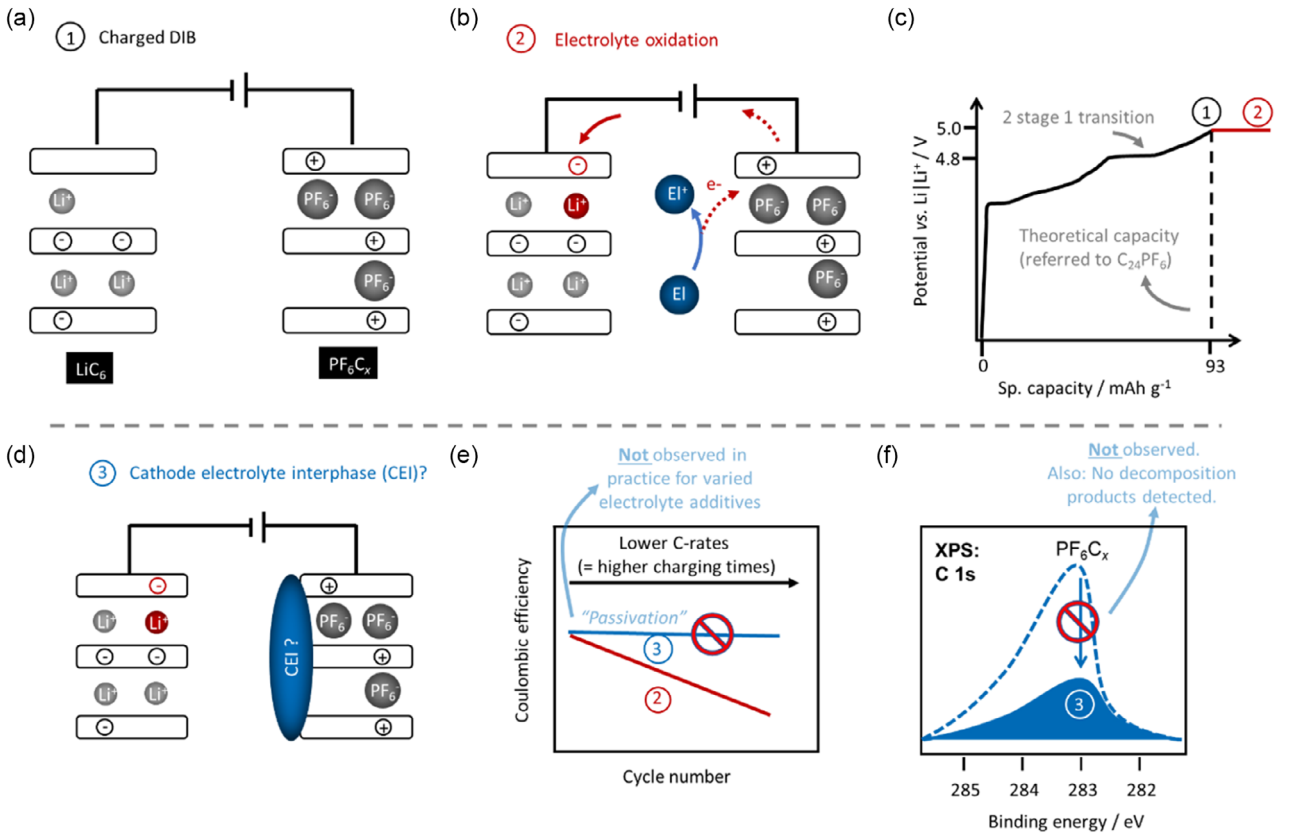

Figure 11. a) After charging a typical DIB (hybrid dual-ion capacitor in the actual case) up to 5 V versus Li|Li^+, b) electrolyte oxidation can proceed leading to c) additional charge capacity beyond the practical sp. capacity of 93 mAh g^{-1}. d) The speculated formation of CEI from electrolyte decomposition products can be negated via e) direct current measurements by decreasing the C rate (i.e., increasing the charging time and facilitating electrolyte oxidation), as seen by decreasing C_{Eff}s. In case of passivating CEI, the C_{Eff} values should remain constantly high. f) XPS analysis also points to an absence of a CEI, as overwhelmingly the GIC surface/composition is visible. In case of CEI, the respective carbon bulk signal should be significantly reduced.

additional surface species and surface coverage are found on the basal plane surface of charged HOPG and on the surface of discharged KS6 graphite electrodes after three and 1000 cycles.

Long-term galvanostatic cycling in graphite || AC half cells with intermittent impedance measurements reveals an average C_{Eff} of 99.74% at 1C from cycle 100 to 1,000 demonstrating good long-term performance. A capacity retention of 94% at 0.1C from the third to the 903th cycle is observed, while the capacity retention at 1C in the 905th cycle referred to the fifth cycle is 85%, which hints on a kinetic origin for capacity fading. By fitting the graphite WE impedance spectra with a transmission line model-based equivalent circuit, an evolving electronic contact resistance, attributed to the particle–particle interfaces in the electrode coating or to the current collector|electrode coating interface, is discovered as major impedance contribution. This interfacial resistance growth is suggested to originate from successive electronic contact loss due to continuous large volume changes during anion de-/intercalation, as illustrated in **Figure 12**. In consequence, the minor capacity loss during long-term cycling may not be mitigated by electrolyte and interphase design strategies; rather, it is likely related with mechanical challenges and to the composite nature of the electrode.

In line with XPS data, no evidence for formation of a CEI on the graphite surface is found by EIS. Analysis of graphite electrodes after 1000 cycles by Raman spectroscopy and XPS does not indicate structural degradation and affirms kinetic hindrance as major contribution for capacity fading.

In conclusion, although the C_{Eff} of graphite || AC half cells slightly rises with charge/discharge cycling, formation of a protective CEI on the PE composed of insoluble inorganic and organic species as found for graphite NEs in LIBs is not observed for the investigated cell and electrolyte formulation. In line with literature for low concentrated $LiPF_6$-based electrolytes or HCEs based on LiTFSI or LiFSI,[11,15] it is assumed that the absence of a CEI on graphite PEs may be also valid for other typically applied electrolyte additives unless CEI formation has been proven explicitly by electrochemical data obtained in, for example, three-electrode cell setups and/or by spectroscopic or microscopy techniques.[12]

Despite absence of CEI, the minor capacity fading indicates reasonable stability of active material even at the high electrode potentials. Cycle number of graphite PEs may be theoretically further extended if the rise in electronic contact resistances can be minimized by, for example, optimization of electrode composite.

The nature of CEI can be concluded to be complex, as it is material and parameter dependent and requires systematic studies for general conclusions. CEI on graphite is shown to be unlikely in this work, which suggests that electrolyte oxidation does not necessarily lead to CEI-forming precipitations of decomposed electrolyte products. Moreover, other cathode materials can be more complicated and additional points need to be considered, for example, native surface layers and nonprotective electrochemical decomposition products.

4. Experimental Section

Electrode Preparation: Graphite PEs were prepared using 93 wt% KS6 graphite (*Imerys Graphite & Carbon*), 2 wt% conductive agent (carbon black C-nergy Super C65, *Imerys Graphite & Carbon*), and 5 wt% sodium

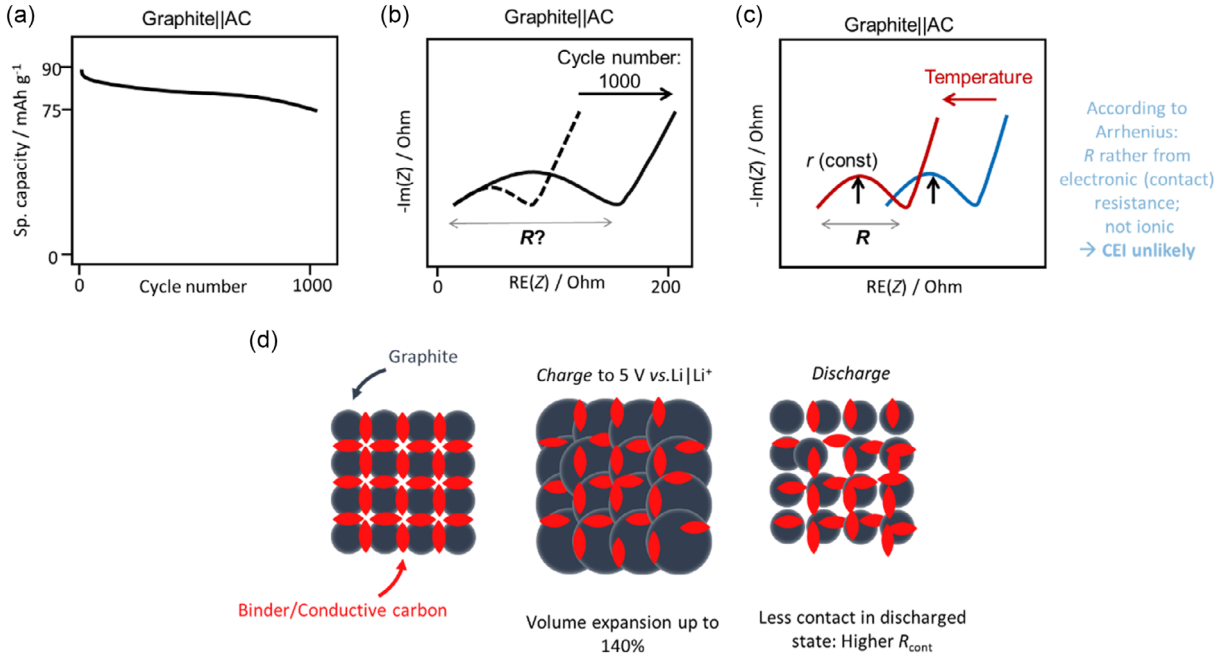

Figure 12. Schematic summary of the capacity fade deconvolution. a) The slight capacity fade after 1000 cycles is shown to be kinetically reasoned. b) The increase of the midfrequency semicircle can be assigned contact resistance. c) Given the remaining radius of the semicircle in course of temperature variations, a low activation energy can be concluded according to Arrhenius law, which is likely the result of electronic resistance. rendering CEI unlikely, as otherwise it would raise ionic resistance. d) The respective resistance rise is suggested to proceed by segregation and particle contact losses of composite network in course of the high volume changes during charge/discharge cycling.

carboxymethylcellulose binder (CMC; Walocel CRT 2000 PPA 12, *Dow Wolff Cellulosics*). The electrode components were dry mixed and then mixed with water forming a suspension with ≈27% solid content. After homogenizing at 10 000 rpm with a Dispermat LC30 (*VMA-Getzmann*), the electrode paste was coated onto Al foil (*Evonik Industries*) with a doctor blade using a gap width of 100 µm. The electrode sheets were dried at 70 °C for 2 h at ambient atmosphere. Electrodes were punched out and dried at 110 °C under reduced pressure ($\leq 5 \times 10^{-2}$ mbar)for ≥6 h. AC electrodes were prepared by mixing AC, 85 wt%), conductive agent (Super C65, 5 wt%), 10 wt% polytetrafluoroethylene (60 wt% suspension in H_2O) with deionized water to obtain a suspension with ≈19% solid content. The resulting paste was cast on aluminum foil with a gap width of 1.5 mm and the solvent was removed in an oven at 70 °C for 2 h under ambient atmosphere. The electrode sheet was then compressed in a calander (*Hohsen*) using a slit width of 550 µm. Afterward, electrode discs were punched out. The active material coating was carefully removed from the aluminum foil and dried at 120 °C under reduced pressure ($\leq 5 \times 10^{-2}$ mbar) for ≥12 h. The average areal active mass loading was ≈23 mg cm^{-2}.

Electrochemical Experiments: Galvanostatic cycling experiments at different specific currents were performed in *Swagelok*-type T-cells in three-electrode configuration on a Maccor4000 battery cycler (*Maccor*) using KS6 graphite electrodes as WE (diameter Ø = 12 mm), AC electrodes as CE (Ø = 12 mm), and Li metal as reference electrode (RE, Ø = 5 mm). The WE potential was controlled (3.4–5.0 V vs Li|Li$^+$, half-cell setup).[66] The AC electrode mass was largely overdimensioned in terms of mass balancing (active mass ≈26 mg at a capacitance of ≈70 F g^{-1}) to ensure that the AC potential was kept within 2.5–3.5 V versus Li|Li$^+$ during cycling. Therefore, it is proposed that oxidative or reductive processes at the CE were negligible during cell operation in order to analyze the impact of electrolyte additives solely on the WE. A comparison in terms of performance using Li metal as CE and potential profiles showing that the AC potential was kept within 2.5–3.5 V versus Li|Li$^+$ is provided in Figure S1, Supporting Information.

T-cells were assembled in an argon-filled glovebox (*MBraun*, H_2O and $O_2 < 1.5$ ppm). A four-layered MS-OZS30 separator (thickness: 4× 30 µm, Ø = 12.5 mm) was placed between WE and CE soaked with 110 µL of electrolyte. The separator side with the ceramic coating was directed toward the WE. The RE was connected to the WE/CE compartment via a three-layered FS 2226 separator (Ø = 8 mm) soaked with 50 µL of electrolyte. Prior to measurements, cells were rested for 6 h.

Long-term galvanostatic cycling and EIS were performed on a VMP3 Potentiostat (*BioLogic*) using three-electrode KS6 || AC PAT cells (*EL Cell*, three-electrode half-cell setup) using electrodes with Ø = 18 mm (active mass loading of WE: (5.1 ± 0.1) mg) and a customized separator inlet with a coaxial metallic Li ring RE and a four-layered MS-OZS30 separator. A constant spring pressure and axially aligned electrodes helped to improve reproducibility and minimize half-cell impedance artefacts. To verify measured half-cell impedances (three-electrode configuration) and to detect potential measurement artefacts, symmetric graphite || graphite cells (two-electrode full-cell configuration)[66] were assembled with pristine or cycled graphite electrodes extracted from cycled graphite || AC PAT cells.

Except for symmetric graphite || graphite cells, all other cells were operated controlling the WE potential (5.0–3.4 V vs Li|Li$^+$, half-cell setup). For cycling experiments with varying currents, three cycles were performed at 10 mA g^{-1} (≙0.1C). Subsequently, different currents were applied according to the inscriptions in the respective diagrams. For long-term cycling experiments, three formation cycles were performed at 10 mA g^{-1}, too. After that, a repeat structure of 100 cycles was applied: The WE was charged at 10 mA g^{-1} to 4.6 V versus Li|Li$^+$. After a rest step of 2 h for stabilization of the potential, EIS was measured (100 kHz–10 mHz, 10 mV amplitude), and 99 cycles were conducted at 100 mA g^{-1} followed by a characterization cycle at 10 mA g^{-1}. This sequence was repeated nine times. For calculation of the average C_{eff} from the 100th to the 1,000th cycle stated in chapter 1.3.3, the 99.9% confidence interval of the average C_{Eff} value was stated (C_{eff} standard deviation $\sigma_s = 0.37\%$).

Postmortem Investigations: ICP-OES: ICP-OES was performed on a Spectro Arcos (*Spectro Analytical Instruments*) with axial plasma viewing. Emission lines of Ni, Al, Fe, and Cr were analyzed, parameters were set according to literature.[67] The aged electrolyte samples were extracted from disassembled separators of KS6 graphite || AC Swagelok cells after 103 cycles via centrifugation.

Raman Spectroscopy: Graphite samples were analyzed using a confocal LabRAM HR evolution Raman microscope (*Horiba Scientific*) equipped with an air-cooled charge-coupled device (CCD) detector. The sample was excited using a green laser (532 nm, 19 mW) adjusted by a 10% filter to 1.9 mW output power with a 600 line/mm grating. Raman spectra were collected over five integrations of 35 s each. Spectra acquisition and data evaluation was performed using the software LabSpec6.6.2 (*Horiba Scientific*). For determination of relative peak area ratios of *D*-band to *G*-band, straight background and integration areas in a range of 1275–1425 and 1500–1600 cm^{-1} were applied.

For the analysis of structural degradation, KS6 graphite samples after formation were obtained from graphite || AC *Swagelok* T-cells cycled for three times at 10 mA g^{-1} (≙0.1C, 3.4–5.0 V vs Li|Li$^+$, half-cell setup). After the third discharge, the potential was hold constant at 3.4 V versus Li|Li$^+$ for 6 h to ensure complete deintercalation of anions. Electrode samples cycled for 1000 cycles were extracted from long-term experiments with KS6 graphite || AC half-cells using PAT cells as described above. After 1000 cycles, the potential was kept constant at 3.4 V versus Li|Li$^+$ for 24 h to ensure complete delithiation. For determination of the peak area ratio between the *D*-band and *G*-bands, signals from three measurement positions were averaged. For the measurements after 1000 cycles, two samples from different cells were analyzed.

Scanning Electron Microscopy: SEM was performed using a Carl Zeiss AURIGA (*Carl Zeiss Microscopy*) equipped with a field-emission gun (acceleration voltage: 3 kV).

X-Ray Photoelectron Spectroscopy: XPS was performed with an Axis Ultra DLD (*Kratos Analytical*). Monochromatic Al Kα X-rays (beam energy = 1486 eV, 12 kV acceleration voltage, 10 mA electron emission current of filament) were applied. For core-level spectra, a pass energy of 20 eV and a step width of 0.1 eV were set at a 0° angle of emission to the surface normal. XPS measurements of charged HOPG were performed without charge compensation via a neutralizer to ensure a correct BE scale, as no proper internal reference was available. For Fermi-level alignment between the highly conducting samples[68] and the spectrometer calibrated with Au $4f_{7/2}$, Ag $3d_{5/2}$, and Cu $2p_{3/2}$ photoemission lines,[69] the samples were directly clamped onto a polished Cu sample holder. To control correct BE-scale calibration of the spectrometer directly after the measurements, Cu 2*p* spectra at a sputter-cleaned position (4 keV Ar$^+$ beam energy, 15 µA extractor current, 300 s) of the bare sample holder were acquired (Cu $2p_{3/2}$ peak (932.62 eV, FWHM: 0.9–1.0 eV).[69] The same procedure was applied for measurements of pristine carbons. The BE scale for measurements of cycled and discharged KS6 graphite samples performed with charge neutralization (BE scale calibrated to the carbon-carbon (CC) sp^2 signal at 284.3 eV) was verified with this method.

SDP was performed using an Ar$^+$-ion gun (0.5 kV, 15 µA extractor current). Peak fitting of XPS spectra was performed using the software CasaXPS (*CASA Software*). In general, peaks were fitted with Voigt-type functions approximated by a product of Gauss and Lorentz functions with 30% contribution of the Lorentz functions (GL(30)) using a Shirley-type background. Signals of graphitic sp^2 hybridized compounds exhibited a higher asymmetry and were therefore fit with the asymmetric Lorentz–Gauss-type 'LF' line shape, which can be adjusted for tailing or fronting. More details can be found in the CasaXPS documentation.[70]

KS6 graphite electrodes after three formation cycles and after 1000 cycles in the discharged state were obtained according to the procedure described for Raman spectroscopy. Charged HOPG samples were obtained from HOPG || AC *Swagelok* T-cells charged to 5.0 V versus Li|Li$^+$ at a low current of 2 mA g^{-1}(≙0.02C, three-electrode half-cell setup). Before disassembly, the WE potential was held at 5.0 V versus Li|Li$^+$ for 12 h. In general, charged and discharged electrodes extracted from cells were directly rinsed with 3× 500 µL of DMC from both sides within 2 min. Samples were mounted on sample holders with adhesive tapes, directly transferred to the XPS chamber and measured after being stored 2 h in the

UHV chamber. At least two graphite samples from different cells were measured at three positions each for all charged/cycled samples to obtain information about the reproducibility. Powder reference compounds were pressed into pellets (Ø = 13 mm) at a pressure of 695 MPa for 30 s using a hydraulic press (*Specac*) and a KB1300M pressing tool (*Maassen Spektroskopie*) cleaned thoroughly in an ultrasonic bath and subsequently with water and acetone to avoid surface contamination. Before pressing, the pressing device was dried at 60 °C in a dry room (dew point < −50 °C) for 30 min. After pressing the powder pellets, they were immediately transferred into the XPS chamber under inert atmosphere.

Supporting Information

Supporting Information is available from the Wiley Online Library or from the author.

Acknowledgements

The authors thank the BMBF for funding the project TransDIB. Verena Naber is gratefully acknowledged for performing supporting inductively coupled plasma-optical emission spectroscopy measurements. Further, the authors thank Andre Bar for graphical support. The content of this study has been published in the Ph.D. thesis of the first author.

Conflict of Interest

The authors declare no conflict of interest.

Author Contributions

Lukas Haneke: conceptualization (lead); investigation (lead); methodology (lead); writing—original draft (lead). **Felix Pfeiffer**: investigation (equal); methodology (equal). **Katharina Rudolf**: investigation (equal); methodology (equal). **Pranti Sutar**: investigation (equal). **Masoud Baghernejad**: investigation (equal); methodology (lead). **Martin Winter**: conceptualization (supporting); funding acquisition (lead); supervision (equal); writing—review & editing (equal). **Tobias Placke**: conceptualization (equal); investigation (equal); supervision (lead); writing—review & editing (equal). **Johannes Kasnatscheew**: Supervision (supporting); writing—review & editing (lead).

Data Availability Statement

The data that support the findings of this study are available from the corresponding author upon reasonable request.

Keywords

composite network resistances, electrolyte oxidation, electronic versus ionic resistance rises, graphitic dual-ion batteries, surface decomposition products

Received: October 21, 2024
Revised: November 21, 2024
Published online: December 11, 2024

[1] T. Placke, A. Heckmann, R. Schmuch, P. Meister, K. Beltrop, M. Winter, *Joule* **2018**, *2*, 2528.
[2] K. V. Kravchyk, M. V. Kovalenko, *Adv. Energy Mater.* **2019**, *9*, 1901749.
[3] O. Fromm, A. Heckmann, U. C. Rodehorst, J. Frerichs, D. Becker, M. Winter, T. Placke, *Carbon* **2018**, *128*, 147.
[4] L. Frankenstein, P. Glomb, J. Ramirez-Rico, M. Winter, T. Placke, A. Gomez-Martin, *ChemElectroChem* **2023**, *10*, e202201073.
[5] T. Placke, O. Fromm, S. F. Lux, P. M. Bieker, S. Rothermel, H.-W. Meyer, S. Passerini, M. Winter, *J. Electrochem. Soc.* **2012**, *159*, A1755.
[6] A. Heckmann, J. Thienenkamp, K. Beltrop, M. Winter, G. Brunklaus, T. Placke, *Electrochim. Acta* **2018**, *260*, 514.
[7] S. Miyoshi, T. Akbay, T. Kurihara, T. Fukuda, A. T. Staykov, S. Ida, T. Ishihara, *J. Phys. Chem. C* **2016**, *120*, 22887.
[8] J. M. Wrogemann, L. Haneke, T. Ramireddy, J. E. Frerichs, I. Sultana, Y. I. Chen, F. Brink, M. R. Hansen, M. Winter, A. M. Glushenkov, T. Placke, *Adv. Sci.* **2022**, *9*, e2201116.
[9] V. Küpers, J. F. Dohmann, P. Bieker, M. Winter, T. Placke, M. Kolek, *ChemSusChem* **2021**, *14*, 4480.
[10] L. Haneke, J. E. Frerichs, A. Heckmann, M. M. Lerner, T. Akbay, T. Ishihara, M. R. Hansen, M. Winter, T. Placke, *J. Electrochem. Soc.* **2020**, *167*, 140526.
[11] A. Kotronia, H. D. Asfaw, C.-W. Tai, M. Hahlin, D. Brandell, K. Edström, *ACS Appl. Mater. Interfaces* **2021**, *13*, 3867.
[12] H. D. Asfaw, A. Kotronia, *Cell Rep. Phys. Sci.* **2022**, *3*, 100693.
[13] W.-H. Li, Y.-M. Li, X.-F. Liu, Z.-Y. Gu, H.-J. Liang, X.-X. Zhao, J.-Z. Guo, X.-L. Wu, *Adv. Funct. Mater.* **2022**, *32*, 2201038.
[14] Z. Cheng, L. Guo, Q. Dong, C. Wang, Q. Yao, X. Gu, J. Yang, Y. Qian, *Adv. Energy Mater.* **2022**, *12*, 2202253.
[15] Y. He, C. Zhen, M. Li, X. Wei, C. Li, Y. Zhu, X. Yang, M. D. Gu, *ACS Nano* **2023**, *17*, 21730.
[16] J. A. Read, *J. Phys. Chem. C* **2015**, *119*, 8438.
[17] G. Homann, L. Stolz, J. Nair, I. C. Laskovic, M. Winter, J. Kasnatscheew, *Sci. Rep.* **2020**, *10*, 4390.
[18] J. Mindemark, M. J. Lacey, T. Bowden, D. Brandell, *Prog. Polym. Sci.* **2018**, *81*, 114.
[19] G. Homann, L. Stolz, K. Neuhaus, M. Winter, J. Kasnatscheew, *Adv. Funct. Mater.* **2020**, *30*, 2006289.
[20] D. Aurbach, K. Gamolsky, B. Markovsky, Y. Gofer, M. Schmidt, U. Heider, *Electrochim. Acta* **2002**, *47*, 1423.
[21] S. Dalavi, P. Guduru, B. L. Lucht, *J. Phys. Energy* **2012**, *159*, A642.
[22] G. H. Wrodnigg, J. O. Besenhard, M. Winter, *J. Phys. Energy* **1999**, *146*, 470.
[23] J. A. Read, A. V. Cresce, M. H. Ervin, K. Xu, *Energy Environ. Sci.* **2014**, *7*, 617.
[24] S. Klein, P. Harte, S. van Wickeren, K. Borzutzki, S. Röser, P. Bärmann, S. Nowak, M. Winter, T. Placke, J. Kasnatscheew, *Cell Rep. Phys. Sci.* **2021**, *2*, 100521.
[25] B. Heidrich, A. Heckmann, K. Beltrop, M. Winter, T. Placke, *Energy Storage Mater.* **2019**, *21*, 414.
[26] J. Kasnatscheew, B. Streipert, S. Röser, R. Wagner, I. Cekic Laskovic, M. Winter, *Phys. Chem. Chem. Phys.* **2017**, *19*, 16078.
[27] S. Rothermel, P. Meister, G. Schmuelling, O. Fromm, H.-W. Meyer, S. Nowak, M. Winter, T. Placke, *Energy Environ. Sci.* **2014**, *7*, 3412.
[28] W. Rüdorff, *Advances in Inorganic Chemistry and Radiochemistry*, Vol. *1* (Eds: H. J. Emeléus, A. G. Sharpe), Elsevier, Amsterdam **1959**, p. 223.
[29] K. Edström, M. Herstedt, D. P. Abraham, *J. Power Sources* **2006**, *153*, 380.
[30] A. M. Andersson, A. Henningson, H. Siegbahn, U. Jansson, K. Edström, *J. Power Sources* **2003**, *119*, 522.
[31] P. Niehoff, S. Passerini, M. Winter, *Langmuir* **2013**, *29*, 5806.
[32] T. Nobuta, T. Ogawa, *J. Mater. Sci.* **2009**, *44*, 1800.
[33] B. Schnyder, D. Alliata, R. Kötz, H. Siegenthaler, *Appl. Surf. Sci.* **2001**, *173*, 221.
[34] G. K. Wertheim, P. T. T. M. van Attekum, S. Basu, *Solid State Commun.* **1980**, *33*, 1127.

[35] G. K. Wertheim, S. B. Dicenzo, *MRS Proc.* **1982**, *20*, 71.
[36] C. R. Brundle, B. V. Crist, P. S. Bagus, *J. Vac. Sci. Technol., A* **2021**, *39*, 13202.
[37] S. B. Dicenzo, S. Basu, G. K. Wertheim, *Synth. Met.* **1981**, *3*, 139.
[38] S. Leroy, F. Blanchard, R. Dedryvère, H. Martinez, B. Carré, D. Lemordant, D. Gonbeau, *Surf. Interface Anal.* **2005**, *37*, 773.
[39] A. M. Andersson, K. Edström, *J. Power Sources* **2001**, *148*, A1100.
[40] K. N. Wood, G. Teeter, *ACS Appl. Energy Mater.* **2018**, *1*, 4493.
[41] J. E. Frerichs, L. Haneke, M. Winter, M. R. Hansen, T. Placke, *J. Power Sources Adv.* **2021**, *12*, 100075.
[42] G. P. López, D. G. Castner, B. D. Ratner, *Surf. Interface Anal.* **1991**, *17*, 267.
[43] D. Pritzl, S. Solchenbach, M. Wetjen, H. A. Gasteiger, *J. Phys. Energy* **2017**, *164*, A2625.
[44] E. Peled, D. Bar Tow, A. Merson, A. Gladkich, L. Burstein, D. Golodnitsky, *J. Power Sources* **2001**, *97*, 52.
[45] T. Placke, O. Fromm, S. Rothermel, G. Schmuelling, P. Meister, H.-W. Meyer, S. Passerini, M. Winter, *ECS Trans.* **2013**, *50*, 59.
[46] S. Tanuma, C. J. Powell, D. R. Penn, *Surf. Interface Anal.* **2005**, *37*, 1.
[47] C. J. Powell, A. Jablonski, *NIST Electron Inelastic-Mean-Free-Path Database: Version 1.2*, National Institute of Standards and Technology, Gaithersburg, MD **2010**.
[48] M. Ue, *J. Electrochem. Soc.* **1994**, *141*, 3336.
[49] J. Landesfeind, D. Pritzl, H. A. Gasteiger, *J. Phys. Energy* **2017**, *164*, A1773.
[50] R. de Levie, *Electrochim. Acta* **1963**, *8*, 751.
[51] J. Bisquert, *Phys. Chem. Chem. Phys.* **2000**, *2*, 4185.
[52] J. O. Besenhard, H. P. Fritz, *Angew. Chem., Int. Ed.* **1983**, *22*, 950.
[53] D. Pritzl, J. Landesfeind, S. Solchenbach, H. A. Gasteiger, *J. Phys. Energy* **2018**, *165*, A2145.
[54] M. D. Levi, D. Aurbach, *J. Phys. Chem. B* **1997**, *101*, 4630.
[55] D. R. Franceschetti, *J. Electroanal. Chem. Interfacial Electrochem.* **1984**, *178*, 1.
[56] J. Bisquert, G. Garcia-Belmonte, P. Bueno, E. Longo, L. O. S. Bulhões, *J. Electroanal. Chem.* **1998**, *452*, 229.
[57] G. J. Brug, A. L. G. van den Eeden, M. Sluyters-Rehbach, J. H. Sluyters, *J. Electroanal. Chem. Interfacial Electrochem.* **1984**, *176*, 275.
[58] B. Hirschorn, M. E. Orazem, B. Tribollet, V. Vivier, I. Frateur, M. Musiani, *Electrochim. Acta* **2010**, *55*, 6218.
[59] N. Ogihara, S. Kawauchi, C. Okuda, Y. Itou, Y. Takeuchi, Y. Ukyo, *J. Phys. Energy* **2012**, *159*, A1034.
[60] G. Schmuelling, T. Placke, R. Schmuch, O. Fromm, H.-W. Meyer, S. Passerini, M. Winter, *J. Power Sources* **2013**, *239*, 563.
[61] A. C. Ferrari, *Solid State Commun.* **2007**, *143*, 47.
[62] A. C. Ferrari, D. M. Basko, *Nat. Nanotechnol.* **2013**, *8*, 235.
[63] R. J. Nemanich, S. A. Solin, D. Gúerard, *Phys. Rev. B* **1977**, *16*, 2965.
[64] M. Balabajew, H. Reinhardt, N. Bock, M. Duchardt, S. Kachel, N. Hampp, B. Roling, *Electrochim. Acta* **2016**, *211*, 679.
[65] A. C. Ferrari, S. E. Rodil, J. Robertson, *Phys. Rev. B* **2003**, *67*, 155306.
[66] R. Nölle, K. Beltrop, F. Holtstiege, J. Kasnatscheew, T. Placke, M. Winter, *Mater. Today* **2020**, *32*, 131.
[67] M. Evertz, J. Kasnatscheew, M. Winter, S. Nowak, *Anal. Bioanal.Chem.* **2019**, *411*, 277.
[68] E. McRae, J.-F. Mareche, *J. Phys. C: Solid State Phys.* **1985**, *18*, 1627.
[69] M. T. Anthony, M. P. Seah, *Surf. Interface Anal.* **1984**, *6*, 95.
[70] N. Fairley, V. Fernandez, M. Richard-Plouet, C. Guillot-Deudon, J. Walton, E. Smith, D. Flahaut, D. Greiner, M. Biesinger, S. Tougaard, D. Morgan, J. Baltrusaitis, *Appl. Surf. Sci. Adv.* **2021**, *5*, 100112.